Journal of The
Electrochemical Society

The Electrochemical Society
Advancing solid state & electrochemical science & technology

Enhanced Battery Performance through Three-Dimensional Structured Electrodes: Experimental and Modeling Study

To cite this article: Jie Li *et al* 2018 *J. Electrochem. Soc.* **165** A3566

View the article online for updates and enhancements.

You may also like

- A Method to Optimize 3D Microbatteries
Kaito Miyamoto
- Mesoscale Electrochemical Performance Simulation of 3D Interpenetrating Lithium-Ion Battery Electrodes
Bradley Trembacki, Eric Duoss, Geoffrey Oxberry et al.
- Recent progress in laser texturing of battery materials: a review of tuning electrochemical performances, related material development, and prospects for large-scale manufacturing
Wilhelm Pfleging

PAT-Tester-x-8 Potentiostat:
Modular Solution for Electrochemical Testing!

EL-CELL®
electrochemical test equipment

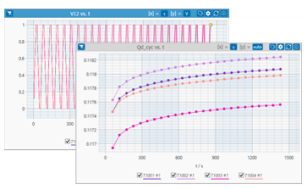

- **Flexible Setup with up to 8 Independent Test Channels!**
Each with a fully equipped Potentiostat, Galvanostat and EIS!
- **Perfect Choice for Small-Scale and Special Purpose Testing!**
Suited for all 3-electrode, optical, dilatometry or force test cells from EL-CELL.
- **Complete Solution with Extensive Software!**
Plan, conduct and analyze experiments with EL-Software.
- **Small Footprint, Easy to Setup and Operate!**
Usable inside a glove box. Full multi-user, multi-device control via LAN.

Scan me!

Contact us:
+49 40 79012-734
sales@el-cell.com
www.el-cell.com

This content was downloaded from IP address 71.61.200.114 on 08/03/2025 at 06:59

Journal of The Electrochemical Society, **165** (14) A3566-A3573 (2018)
0013-4651/2018/165(14)/A3566/8/$37.00 © The Electrochemical Society

Enhanced Battery Performance through Three-Dimensional Structured Electrodes: Experimental and Modeling Study

Jie Li,[1] Xinhua Liang,[2,*] Rahul Panat,[3] and Jonghyun Park[1,*,z]

[1]*Department of Mechanical and Aerospace Engineering, Missouri University of Science and Technology, Rolla, Missouri 65401, USA*
[2]*Department of Chemical and Biochemical Engineering, Missouri University of Science and Technology, Rolla, Missouri 65409, USA*
[3]*Department of Mechanical Engineering, Carnegie Mellon University, Pittsburgh, Pennsylvania 15213, USA*

Three-dimensional (3D) electrode structures have the potential to significantly improve Li-ion battery performance, including power and energy density. Due to the complexity of geometries caused by scale expansion, however, a more precise understanding of the relationship between battery physics and structures is required. In this work, a novel hybrid 3D structure is investigated to thoroughly understand the advantages of 3D structured electrodes and to provide a guideline for design optimization. Experimental observation from an extrusion-based 3D structure is incorporated into a 3D electrochemical model, based on porous theory, with a 4th order approximation for solid phase concentration. This systematic study has been focused on the impact of electrode tap density (thickness and volume fractions) on 3D battery performance. Experimental and simulation results showed that the proposed 3D hybrid structure exhibited higher specific capacity and areal capacity than conventional electrode structures. This was found to be due to the short diffusion path and uniformly distributed concentration within the electrodes, even with thicker electrodes. Parametric metrics were introduced to provide a physical insight into the 3D hybrid structure, to identify the factors limiting battery responses, and to, eventually, provide a guideline for design optimization with more general 3D geometries.
© 2018 The Electrochemical Society. [DOI: 10.1149/2.1351814jes]

Manuscript submitted August 9, 2018; revised manuscript received November 9, 2018. Published November 17, 2018.

Advanced Li-Ion Batteries (LIBs) are one of the key solutions to the challenges associated with pollution and transportation energy costs. The development of an advanced battery at a reduced cost requires optimal battery design, which allows for minimizing unnecessary components that increase both the weight and the cost. In order to optimize battery design, besides developing new materials, it is necessary to enhance battery performance via optimizing battery electrode structures to promote the transport of species and their reactions.[1–5] Although gravimetric capacity is one of the most utilized metrics in LIB studies, as it describes the capacity of a material's delivery, the actual amount of materials in an electrode determines the energy and power of the LIB. Therefore, a high tap density is another important requirement for various applications.

Adding more material, which is a simple method for achieving high tap density, can be fulfilled by increasing the thickness or volume fraction of electrodes. Conventional laminated composite electrodes are fabricated via a tape casting process that involves mixing the constituent materials and casting them onto a current collector. Although tap density increases with increasing electrode thickness, after a certain thickness is attained, the battery performance becomes poor. This is due to the limitation of the transport of ions that causes poor utilization of materials.[1] A better way to increase tap density, without sacrificing power, is to fabricate electrodes that can allow a more facile transport of the species.[2–5] Three-dimensional (3D) battery architectures have been considered to be a new solution for this approach. Currently, it has been confirmed that the 3D structure of batteries can efficiently improve the utilization of materials.[5–11] In our previous work, a novel hybrid 3D electrode structure was developed that enhanced areal energy and power densities by overcoming the tradeoff between specific capacity and areal capacity.[5,6]

Optimal battery design via modeling is one of the most effective ways, in terms of reducing processing time and costs, compared to experimental approach. Modeling tools for these purposes, however, must include appropriate design elements and be accurate in predicting results. In recent decades, researchers have developed computational models that simulate a 3D structure based on non-porous electrode theory as a thin film model.[12–16] Those models might accurately account for geometry in nano-/micro-scale (particle-level), but are computationally too expensive to consider for mesoscale (cell-level) battery structures, and are limited to those types of batteries. To simulate batteries in mesoscale, the pseudo-2D (P2D) model[17] has been widely used for predicting battery performance. This model relies on the continuum-based porous electrode theory, which is also able to study the effects of different active material compositions on power and energy performance,[18] as well as mechanical stress in particles when a cell is subjected to a mechanical load.[19] This method is, however, limited to the study of homogenized systems and, therefore, it cannot account for the effects of the geometry of an electrode on battery cell performance. Another mathematical model in 1D, called Single Particle model,[20] is a reduced order model based on the P2D model with an analytical expression for the solid phase concentration. Although those models are not able to capture non-uniform geometry on a large scale, they can quite accurately predict battery behavior.

In this paper, a 3D physical based electrochemical model is proposed, based on the porous electrode theory, to solve the transport and kinetics problems of arbitrary 3D electrode structures. This 3D model utilized the full order P2D model with replacing the partial differential equation of Fick's laws to a fourth order analytical solution for the solid phase diffusion problem, and then the results were validated through experiments. An additional case study consisting of the effect of thickness on battery performance has provided a better understanding of the benefits of 3D structures as compared to conventional laminated structures. Numerical simulation results have included detailed electrochemical behaviors of the geometric effects on battery cell performance, including solid phase concentration distribution, voltage profiles, and specific capacity. Further, the limiting factors of an electrode structure were introduced and, based on this, the guidelines to obtain optimal parameters were investigated and determined.

Experimental and Simulation Method

Materials preparation, electrode fabrication, and test.—In this work, a $LiMn_2O_4$ (LMO) paste was used to fabricate electrodes. A 30% solids loading paste was prepared by mixing 85.5 wt% LMO powder (MTI, 13 μm) with 6.5 wt% carbon black (CB, Alfa Aesar) and 8 wt% Polyvinylidene fluoride (PvdF, Sigma-Aldrich) in N-Methyl-2-pyrrolidone solvent (NMP, Sigma-Aldrich). An extrusion-based additive manufacturing system was used to extrude the paste into a 3D structure. A piece of aluminum foil was fixed on a substrate (heated to 120 °C prior to printing), which was used as a current collector after assembly. The paste was loaded into a plastic syringe with a 200 μm nozzle and extruded onto a substrate that moved along the

*Electrochemical Society Member.
[z]E-mail: parkjonghy@mst.edu

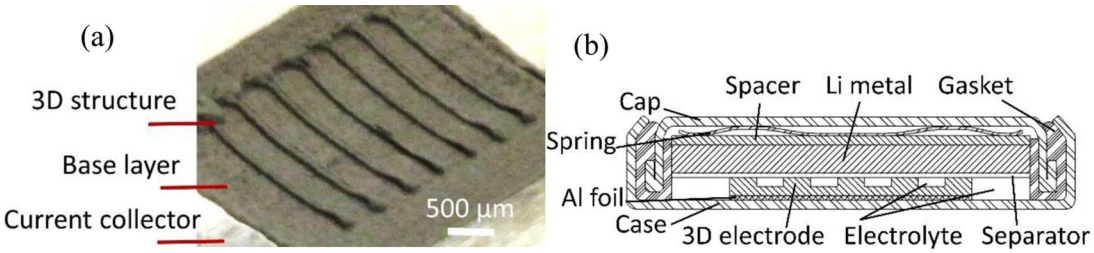

Figure 1. (a) Microscopic image of printed hybrid 3D structure and (b) A CR2032 coin cell assembly with hybrid 3D structure cathode, Li foil, separator, and electrolyte.

XY-axes. The hybrid 3D structure consisted of two parts: a base part and a digital structure part (Figure 1a). First, a base layer was printed to cover the current collector as a conventional laminated structure; the thickness of this base layer was optimized to yield the highest specific capacity (without a 3D structure). Next, a digital structure, with a different number of layers, was printed on the top of the base layer to increase the specific surface area.

A CR2032 coin cell was used to assemble a battery (Figure 1b) in an argon-filled glove box. LMO was used as a cathode, Li foil as an anode, and commercial PP/PE/PP membrane as a separator; the battery was filled with liquid electrolyte 1M $LiFP_6$ EC:DMC 1:1 (Sigma-Aldrich). The electrochemical behavior of the assembled batteries was measured from 3 V to 4.2 V. The specific capacity and areal capacity were measured under a 0.1 C-rate.

Continuum electrochemical model for Li-ion batteries.—A 3D half-cell model was developed by considering the mass and charge conservation equations, and the corresponding boundary conditions, as shown in Figure 2. All governing equations were derived from the porous electrode theory.

Transport in solid phase.—Inside the active material of each electrode, the solid phase Li-ion concentration can be described by Fick's law in a spherical coordinate,

$$\frac{\partial c_{s,j}(r,t)}{\partial t} = \frac{D_{s,j}}{r^2}\frac{\partial}{\partial r}\left(r^2\frac{\partial c_{s,j}(r,t)}{\partial r}\right) \quad [1]$$

where $c_{s,j}$ is the solid phase Li-ion concentration, t is time, r is the radial coordinate, $D_{s,j}$ is the solid phase diffusion coefficient, and the subscript $j = p/n$ denotes the positive/negative electrode. The boundary condition for Eq. 1 is:

$$D_{s,j}\left.\frac{\partial c_{s,j}(t)}{\partial r}\right|_{r=0} = 0 \; and \; D_{s,j}\left.\frac{\partial c_{s,j}(t)}{\partial r}\right|_{r=R_j} = -J_j(t) \quad [2]$$

where R_j is the particle radius and J_j is the Li-ion molar flux density on the active material surface.

In this work, a 4th order polynomial approximation is used to consider the solid phase concentration, which has been well established based on a volume-averaging assumption. The solid phase concentration can be described as[20]

$$c_{s,j}(r,t) = a(t) + b(t)\left(\frac{r^2}{R_j^2}\right) + c(t)\left(\frac{r^4}{R_j^4}\right) \quad [3]$$

By substituting the polynomial approximation in Eq. 3 to Eq. 1, the coefficients $a(t)$, $b(t)$, and $c(t)$ are, respectively,

$$a(t) = \frac{39}{4}c_{s,j,surf}(t) - 3R_j q_{s,j,avg}(t) - \frac{35}{4}c_{s,j,avg}(t) \quad [4a]$$

$$b(t) = -35c_{s,j,surf}(t) + 10R_j q_{s,s,avg}(t) + 35c_{s,j,avg}(t) \quad [4b]$$

$$c(t) = \frac{105}{4}c_{s,j,surf}(t) - 7R_j q_{s,s,avg}(t) - \frac{105}{4}c_{s,j,avg}(t) \quad [4c]$$

where $c_{s,j,surf}$ is the particle surface concentration, $c_{s,j,avg}$ is the average solid phase concentration, and $q_{s,j,surf}$ is the average solid phase flux. Using the boundary conditions in Eq. 2, after substituting the polynomial approximation in Eq. 3 into Eq. 1, the following ODEs were obtained to describe the average solid-phase concentration and average solid-phase flux, respectively:

$$\frac{dc_{s,p,avg}(X,t)}{dt} = -\frac{J_p(X,t)}{3R_p} \quad [5]$$

$$\frac{dq_{s,p,avg}(X,t)}{dt} = -30\frac{D_{s,p}}{R_p^2}q_{s,p,avg}(X,t) - \frac{45}{2R_p^2}J_p(X,t) \quad [6]$$

where $\boldsymbol{X}$ is the coordinate (x, y, and z) inside 3D electrode (as shown in Fig. 2). Then, the particle surface concentration inside the cathode can be expressed as

$$c_{s,p,surf}(X,t) = c_{s,p,avg}(X,t) + \frac{8R_p}{35}q_{s,p,avg}(X,t) - \frac{R_p}{35D_{s,p}}J_p(X,t) \quad [7]$$

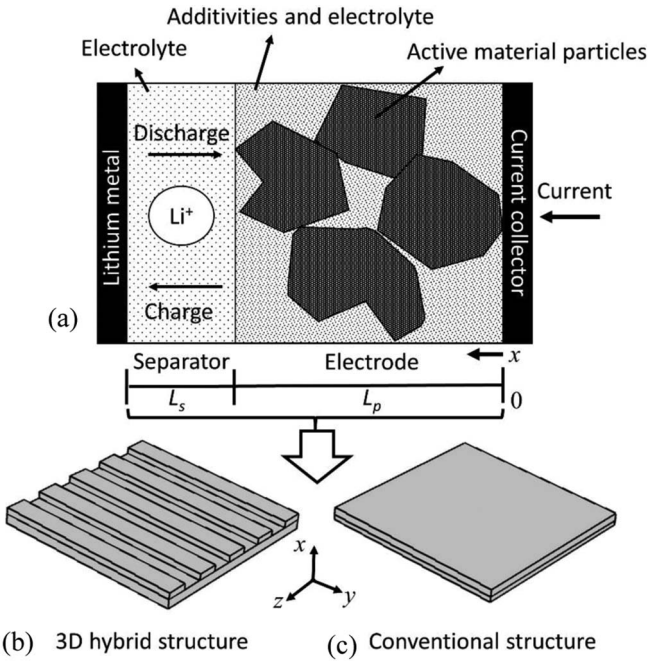

Figure 2. (a) Illustration of cell with porous electrode, (b) 3D hybrid structure, and (c) conventional structure.

The Li-ion molar flux density is related to the individual electrode's over potential through Bulter-Vomer kinetics

$$J_p(X,t) = k_p c_{s,p,max} c_e^{0.5} \left(1 - \frac{c_{s,p,surf}(X,t)}{c_{s,p,max}}\right)^{0.5} \left(\frac{c_{s,p,surf}(X,t)}{c_{s,p,max}}\right)^{0.5} \times \left\{exp\left(\frac{0.5F}{RT}\eta_p(X,t)\right) - exp\left(-\frac{0.5F}{RT}\eta_p(X,t)\right)\right\} \quad [8a]$$

For the lithium electrode at $x = L_s + L_p$ (Figure 2a)

$$J_{Li}(t) = 0.85\left\{exp\left(-\frac{0.5F}{RT}\Phi_{e,s}(X,t)\right) - exp\left(\frac{0.5F}{RT}\Phi_{e,s}(X,t)\right)\right\} \quad [8b]$$

where k_p is the reaction rate constant, c_e is the electrolyte concentration, R is the universal gas constant, T is the ambient temperature, and η_j is the reaction overpotential defined as $\eta_p = \Phi_{s,p} - \Phi_{e,p} - U_p$, where $\Phi_{s,p}$ is the solid-phase potential, $\Phi_{e,p}$ is the electrolyte phase potential, and U_p is the open-circuit potential (OCP), which is generally a function of $c_{s,p,surf}$.

Transport in electrolyte.—The Li-ion concentration in the electrolyte phase changes due to changes in the gradient diffusive flow of Li-ions. The equation is based on the porous electrode theory.[17]

$$\epsilon_k \frac{\partial c_{e,k}(X,t)}{\partial t} = \frac{\partial}{\partial X}\left(D_{eff,k}\frac{\partial c_{e,k}(X,t)}{\partial X}\right) + a_k(1-t_+)J_k(X,t) \quad [9]$$

where $k = p/s$ for cathode and separator, respectively, and $J_s(X,t) = 0$. ε_k is the solid phase volume fraction, $D_{eff,k}$ is the effective electroyte diffusion coefficient, $D_{eff,k} = D_e(1\text{-}\varepsilon_k\text{-}0.26)^{brug}$, $brug$ is the Bruggman coefficient, 1.5, a_k is the specific surface area of electrode, t_+ is the transference number in the electrolyte. The boundary conditions are:

1. Fluxes of the ions are zero for all time at the current collector ($x = 0$ and $x = L_p + L_s$)

$$-D_{eff,p}\frac{\partial c_{e,p}(t)}{\partial X}\bigg|_{x=0} = 0 \quad [10a]$$

$$-D_{eff,s}\frac{\partial c_{e,s}(t)}{\partial X}\bigg|_{x=L_p+L_s} = \frac{J_{Li}(t)}{F} \quad [10b]$$

where L_p is cathode thickness and L_s is separator thickness. The Li-ion concentration in the electrolyte phase changes due to the changes in the gradient diffusive flow of Li-ions. The equation is the same as that in the porous electrode theory.

2. Continuity of the flux and concentration of the electrolyte at the electrode-separator interface

$$-D_{eff,p}\frac{\partial c_{e,p}(t)}{\partial X}\bigg|_{x=L_p} = -D_{eff,s}\frac{\partial c_{e,s}(t)}{\partial X}\bigg|_{x=L_p} \quad [11]$$

$$c_{e,p}(t)\big|_{x=L_p} = c_{e,s}(t)\big|_{x=L_p} \quad [12]$$

The initial condition for Eq. 9 is

$$c_{e,k}(X,0) = c_{e,k,0} \quad [13]$$

The specific electrode surface area, a_p, can be expressed in terms of the solid phase volume fraction in cathode, ε_p, as

$$a_p = \frac{3\varepsilon_e}{R_p} \quad [14]$$

Electrical potentials.—Charge conservation in the solid phase of each electrode can be described by Ohm's law

$$k_{eff,j}\frac{\partial^2\Phi_{s,j}(X,t)}{\partial X^2} = a_j F J_j(X,t) \quad [15]$$

The boundary conditions at the current collectors, as a function of applied current density, I

$$-k_{eff,p}\frac{\partial\Phi_{s,p}(t)}{\partial X}\bigg|_{x=0} = I \quad [16]$$

$$-k_{eff,p}\frac{\partial\Phi_{s,p}(t)}{\partial X}\bigg|_{x=L_p} = 0 \quad [17]$$

where the current density I is related to the applied current, i_{app}, and the electrode foot area, A, as $I = i_{app}/A$, and $k_{eff,k}$ is the effective conductivity as a function of electrolyte concentration $k_{eff,k} = k_k(\varepsilon_k)^{1.5}$. Combining Kirchhoff's law with Ohm's law in the electrolyte phase yields

$$k_{eff,k}\frac{\partial^2\Phi_{e,k}(X,t)}{\partial X^2} - \frac{2k_{eff,k}RT(1-t_+)\partial^2\ln c_{e,k}(X,t)}{F\partial X^2} \times \left(1 + \frac{d\ln f_+}{d\ln c_{e,k}}\right) = I \quad [18]$$

Since the boundary conditions of $\Phi_{e,k}$ are arbitrary. Set $\Phi_{e,k}(0, y, z, t) = 0$ at the positive electrode current collector interface. The remaining boundary conditions follow in continuity of $\Phi_{e,k}$

$$k_{eff,k}\frac{\partial\Phi_{e,k}(X,t)}{\partial X} - \frac{2k_{eff,k}RT(1-t_+)\partial\ln c_{e,k}(X,t)}{F\partial X} \times \left(1 + \frac{d\ln f_+}{d\ln c_{e,k}}\right)\bigg|_{x=0} = 0 \quad [19a]$$

$$k_{eff,k}\frac{\partial\Phi_{e,k}(X,t)}{\partial X} - \frac{2k_{eff,k}RT(1-t_+)\partial\ln c_{e,k}(X,t)}{F\partial X} \times \left(1 + \frac{d\ln f_+}{d\ln c_{e,k}}\right)\bigg|_{x=L_p+L_s} = J_{Li}(t) \quad [19b]$$

$$-k_{eff,p}\frac{\partial\Phi_{e,p}(t)}{\partial X}\bigg|_{x=L_p} = -k_{eff,s}\frac{\partial\Phi_{e,s}(t)}{\partial X}\bigg|_{x=L_p} \quad [20]$$

The governing equations listed above are solved numerically via COMSOL 4.3a, and the parameters used in the simulation are listed in Table I. The battery geometry information, such as particle radius, electrode thickness, and volume fractions, are based on experiments and physical parameters, including diffusivity and conductivity, which are based on common material properties.

Results and Discussion

Experimental observation of electrochemical behavior of printed electrodes.—Battery performances of the conventional structure (CS) and the 3D hybrid structure (HS) were compared at different electrode thicknesses. In the case of specific capacity (Figures 3a and 3b), the CS exhibited a maximum value (110 ± 5 mAh $\cdot$ g^{-1}) at 160 μm, and then decreased as the thickness increased. However, the HS showed a higher value (117 ± 6 mAh $\cdot$ g^{-1}) than that of the CS, even though it was much thicker (270 μm vs. 160 μm). As in the case of CS, the specific capacity of the HS decreased from its maximum value as the thickness of the electrode increased. On the other hand, as the thickness increased (Figures 3a and 3c), the areal capacity of the CS continuously increased, up to a maximum value (3.5 ± 0.08 mAh $\cdot$ cm^{-2} at 270 μm), which was much smaller than the maximum of HS, 4.5 ± 0.3 mAh $\cdot$ cm^{-2} at 270 μm (as shown in Figures 3a and 3c). This was attributed to competition between the increased mass loading and the reduced specific capacity, as the thickness increased.

Table I. Model parameters used in simulation studies.

Parameter	Value	Description
brug	1.5	Bruggeman coefficient
$C_{e,k,0}$	2000	Initial electrolyte concentration (mol m^{-3})
$C_{\max,\,pos}$	16000	Positive maximum concentration (mol m^{-3})
D_e	7.5×10^{-11}	Diffusion coefficient in electrolyte ($m^2 s^{-1}$)
$D_{s,p}$	2.5×10^{-15}	Solid-phase Li diffusivity, positive electrode ($m^2 s^{-1}$)
E_p	10	Young's modulus of the LMO material (GPa)
F	96487	Faraday's constant (C mol^{-1})
i_0	0.85	Constant flux for half-cell
I	Variable	Applied current density (A m^{-2})
$k_{s,p}$	3.8	Solid phase conductivity (S m^{-1})
k_p	2×10^{-6}	Reaction rate coefficient, cathode ($m^{2.5} mol^{-0.5} s^{-1}$)
L_p	Variable	Cathode thickness (m)
L_s	30×10^{-6}	Separator thickness (m)
R	8.314	Universal gas constant (J mol^{-1} K^{-1})
R_p	13×10^{-6}	Particle radius, positive electrode (m)
t_+	0.363	Cationic transport number
ε_p	Variable	Solid phase volume fraction of positive electrode
ε_s	0	Solid phase volume fraction of separator
ν_p	0.3	LMO Poisson's ratio
Ω_p	3.5×10^{-6}	Partial molar volume of solute ($m^3 mol^{-1}$)

Parametric study for insight into the superiority of 3D structures.—Before discussing the details of 3D simulation results, a simple analytical study was conducted by focusing on transportation in the solid and electrolyte phases. The good utilization of the active materials inside the electrode is an important factor to optimize the cell performance. For a desired battery performance, the terminal voltage, V, should below its cutoff value only when all of the active material was consumed/occupied. To achieve this, it is necessary to understand the transport limitations at each phase of the composite electrode, since this leads to non-uniform distribution of reactions.[21] Solid phase diffusion in the active material particles and the electrolyte transportation were two important factors in determining reactions in the 3D electrode and battery performance. To evaluate the relative characteristic times of intercalation and electrolyte transport in relation to the discharge time, two parameters (S_c and S_S) are commonly used for solid phase diffusion and electrolyte transport, respectively.[21] In this work, those two parameters were extended to study the effects of thickness and solid phase volume fraction on conventional and 3D electrodes (shown in Figures 4a and 4b).

For the conventional structure, the S_c is the ratio of diffusion time to discharge time

$$S_{c,con} = \frac{R_p^2 I}{D_{s,p} F \varepsilon_p c_{max,pos} l_{pos}} \quad [21]$$

The S_s is the ratio of electrolyte transport time to discharge time

$$S_{s,con} = \frac{\left(l_{sep} + l_{pos}\right) I w}{D_{eff,p} F \varepsilon_p c_{max,pos} l_{pos}} \quad [22]$$

For 3D structure, to simply the calculation, the effect of the side of the finger structure is ignored and the average length of the cathode is used. Then, Eqs. 21 and 22 can be rewritten as:

$$S_{c,3D} = \frac{R_p^2 I \left(2n - 1\right)}{D_{s,p} c_{max,pos} \varepsilon_p F \left(n l_{pos,1} + \left(n - 1\right) l_{pos,2}\right)} \quad [23]$$

where n is the number of fingers in the 3D structure and $l_{pos,1}$ is the thickness of finger structure and $l_{pos,2}$ is the base structure, w is the length of electrode, as shown in Figure 4b.

$$S_{s,3D} = \frac{\left(n\left(l_{pos,1} + l_{sep}\right) + \left(n - 1\right)\left(l_{pos,2} + l_{sep}\right)\right) w I}{D_{eff,p} c_{max,pos} \varepsilon_p F \left(n l_{pos,1} + \left(n - 1\right) l_{pos,2}\right)} \quad [24]$$

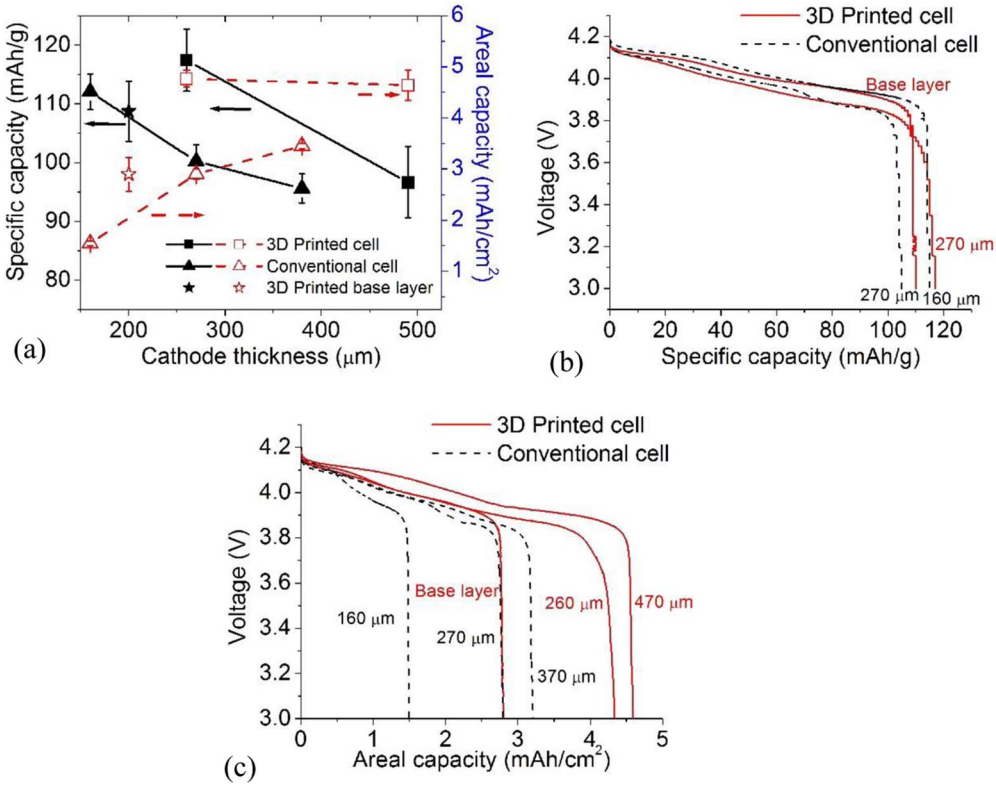

Figure 3. Comparison of a conventional structure and a printed 3D hybrid structure: (a) specific capacity and areal capacity as a function of cathode thickness, voltage profile at different electrode thicknesses as a function of specific capacity, and (c) voltage profile as a function of areal capacity.

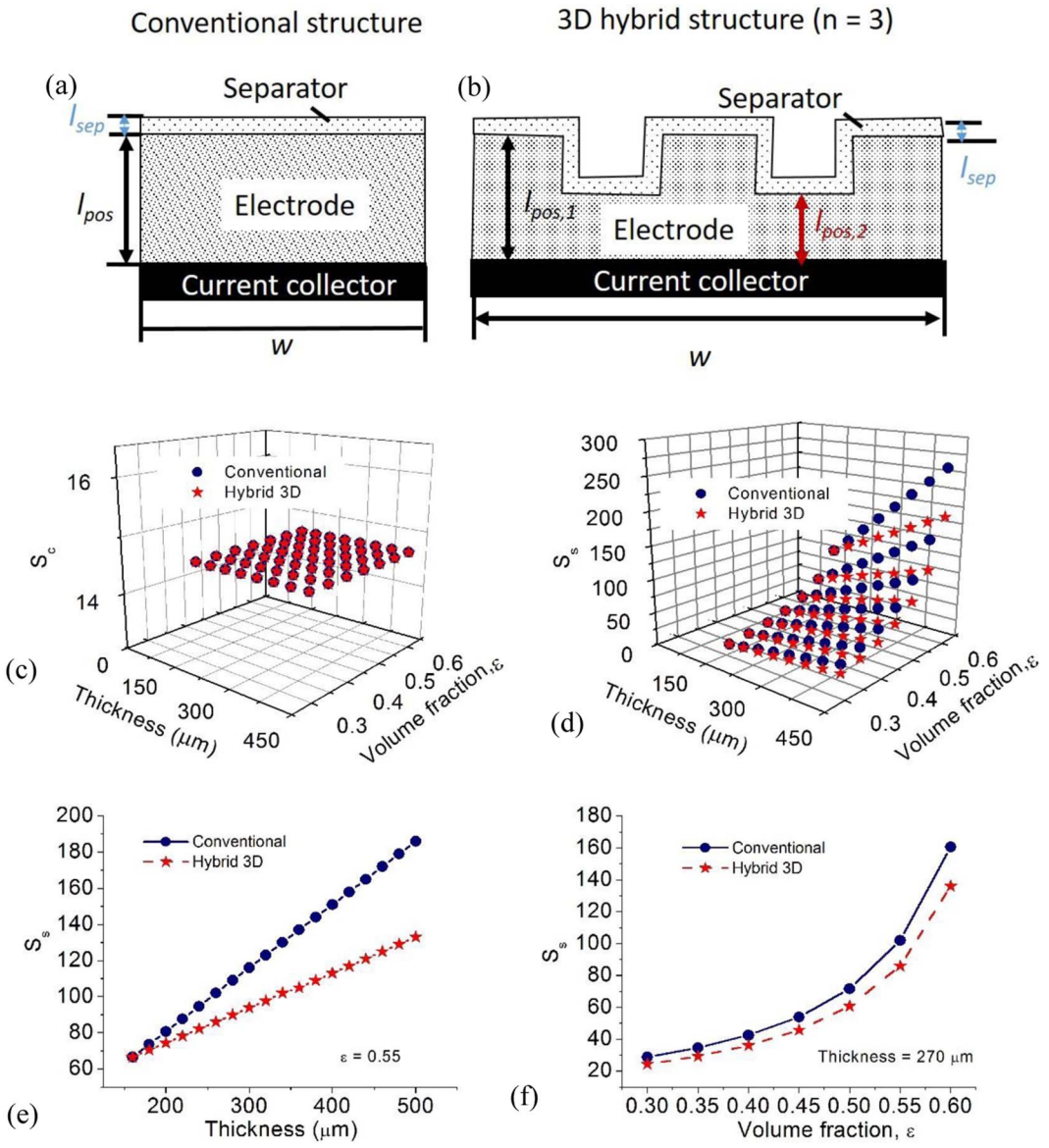

Figure 4. Schematic diagram of (a) conventional structure and (b) 3D hybrid structure; (c) S_c as a function of volume fraction and cathode thickness, (d) S_s as a function of volume fraction and cathode thickness, (e) S_s as a function of thickness with 0.55 volume fraction, and (f) S_s as a function of volume fraction at 270μm thickness.

The current density can be calculated based on theoretical capacity with applied C-rate

$$I = \frac{i_{app}}{A} = \frac{Q_c \varepsilon_p \rho V C_{rate}}{A} = \frac{Q_c \varepsilon_p \rho A l_{pos} C_{rate}}{A} \quad [25]$$

where Q_c is the theoretical battery capacity, ρ is the active material density, V is the electrode volume.

According to Doyle et al.,[21] the case of $S_c >> 1$ means that the diffusion in the solid phase is the limiting factor for battery performance, while for $S_s >> 1$, the transportation concentration variation is the limiting factor. In this study, the S_c and S_s were compared with different volume fractions, from 0.3 to 0.6, and to different cathode thicknesses, from 160 to 500 μm. Both S_c and S_s were limiting factors ($>>1$) with variable thicknesses and volume fractions; the increase in S_c and S_s values meant that the solid phase diffusion or the electrolyte transportation was a more critical factor. As shown in Figure 4c, the value of S_c was independent of the cathode thickness and volume fraction of both the conventional and hybrid 3D structures. This was because S_c is only limited by particle radius, R_p, and solid phase diffusion coefficient, by $D_{s,p}$ (Eqs. 21 and 23). This can be confirmed by Eqs. 21 and 23 in which the terms related to geometry will be cancelled out when Eq. 25 is applied. Whereas the electrolyte transportation was limited by electrode geometry and depended on the volume fraction and electrode thickness (Eqs. 22 and 24).

As shown in Figure 4d, the S_s value increased nonlinearly as a function of volume fraction and linearly as a function of electrode thickness. The S_s value was detailed in Figures 4e and 4f, for a variable thickness with a 0.55 volume fraction and a variable volume fraction at 270μm thickness. Comparing the S_s of the conventional and 3D hybrid structures, it can be seen that the 3D hybrid structure was able to improve electrolyte transportation and was more efficient when thick (maximum reduction 33%) and an approximate reduction of 12% at any volume fraction. This analysis explained how the 3D hybrid structure could improve battery performance when thicker and could be further used to optimize the design of 3D structures.

3D electrochemical model results.—The developed 3D model was first verified with the P2D model,[17] in terms of voltage profile and the solid phase surface concentration at the cathode-separator and cathode-current collector (C.C.) interfaces, respectively. As shown

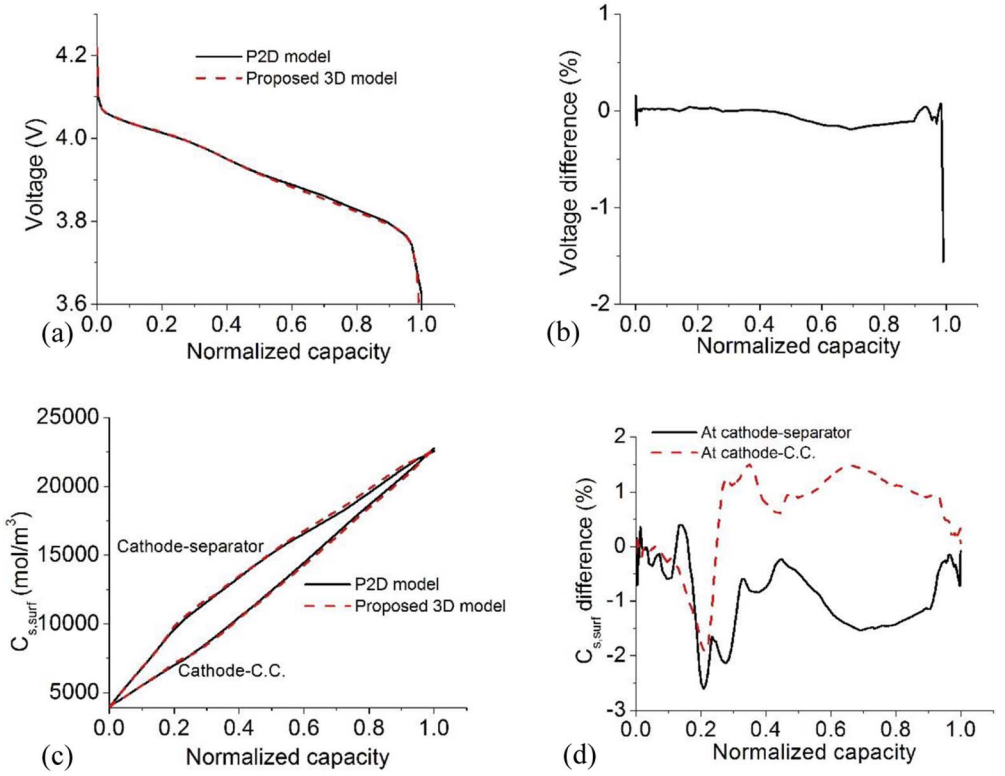

Figure 5. (a) Comparison of voltage profiles from the P2D and the 3D model, (b) voltage difference between them, (c) comparison of solid phase surface concentrations at the cathode-separator and cathode-current collector interfaces from the P2D and the 3D model, and (d) concentration difference between them.

in Figures 5a and 5b, the voltage profile of the 3D model was well matched, at the end of discharge, with the ones from the P2D model. The error rate was smaller than 0.3%. The increased voltage error at the end of discharge could have been due to the 3D model's faster voltage drop after 3.7V, as compared to that of the P2D model. For the solid phase surface concentration (shown in Figures 5c and 5d), the $c_{s,surf}$ of the 3D model at two interfaces agreed well with that of the P2D model, with only a maximum 2% difference. This indicated that, by combining the 4th order approximation equation for solid phase concentration with the P2D model, the model could be extended into three dimensions, with ignorable errors.

Next, the 3D computational model was validated with experimental results by comparing the voltage profiles of a hybrid 3D structure and a conventional structure of 270 μm thickness (as shown in Figure 6a). In general, the model captured capacity change, depending on geometry. Some small deviation might have been related to input parameters.

Next, the 3D model was used to compare capacity change for a 3D hybrid structure (HS) and a conventional structure (CS), as a function of cathode thickness. As shown in Figure 6b, the simulation captured the decrease in capacity with an increase in electrode thickness of from 160 to 490 μm. An experimental observation of the simulation for the CS showed a similar capacity change, from 160 μm to 270 μm. At greater thickness, however, the capacity quickly decreased in the simulation, which could have been due to the limited electrolyte transportation, as mentioned above. The experimental results showed less capacity loss that might have been related to a porous electrode where the electrolyte transportation was not ideally limited, as in the simulation. For the hybrid 3D structure, the simulation agreed well with experimental results at 270 and 160 μm. The capacity decrease, due to increased thickness, showed a less critical phenomena than experiments at 490 μm did, which indicated that a better controlled 3D structure could further improve battery performance.

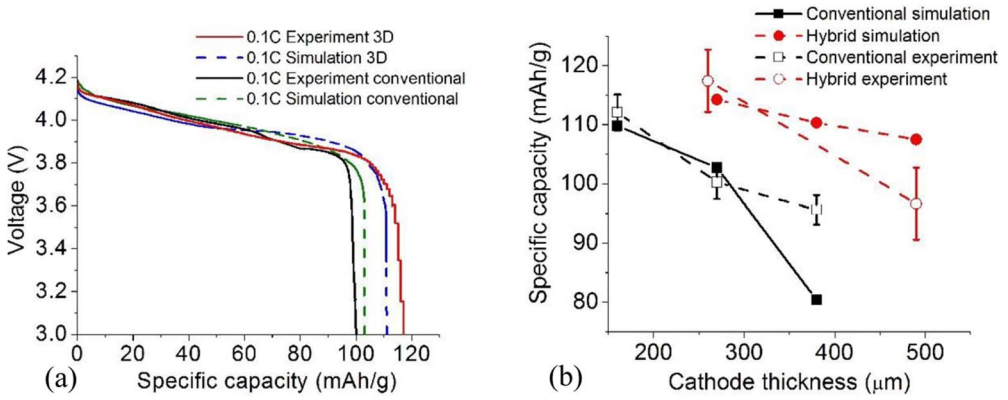

Figure 6. Comparison of (a) voltage profile with simulation and experimental results and (b) specific capacity, as a function of electrode thickness.

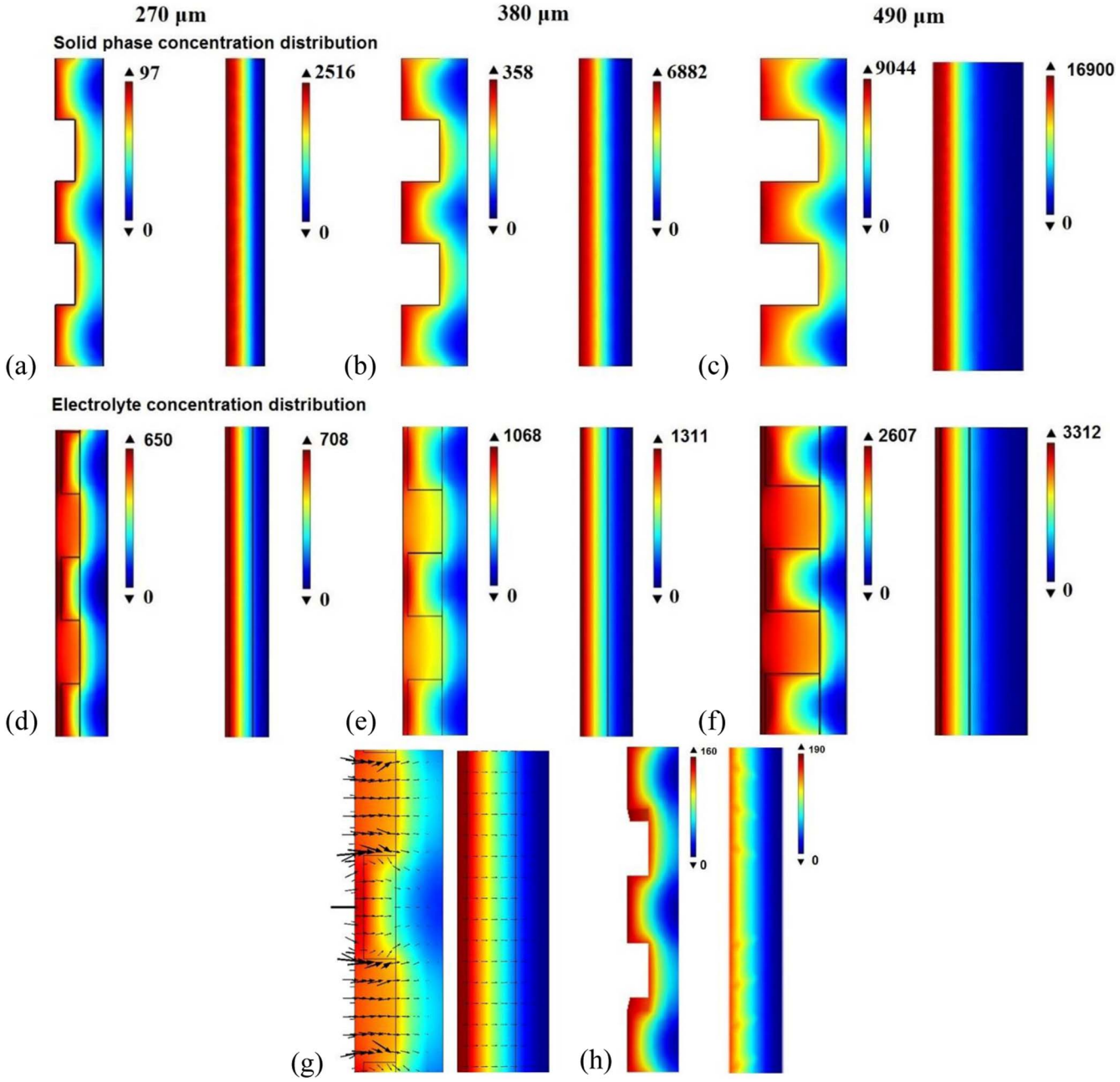

Figure 7. Comparison of concentration distribution (mol/m^3) as a function of thickness of solid phase concentration at (a) 270 µm, (b) 380 µm, and (c) 490 µm; electrolyte concentration (mol/m^3) at (d) 270 µm, (e) 380 µm, and (f) 490 µm; (g) flux distribution and (h) tangential stress distribution (MPa) of the 270 µm thickness electrodes.

In order to examine the reason for the higher capacity of the HS, as compared to that of the CS, Li-ion concentration distributions in the solid and electrolyte phases, at different thicknesses, were compared (shown in Figure 7). First, the concentration gradient increased with increased thickness for both the 3D hybrid and the conventional structures. For the conventional structure, from 270 to 490 µm, the solid phase concentration difference between the electrode-separator interface and the electrode-current collector (C.C) interface increased from 2516 to 16900 mol/m^3; the electrolyte concentration difference between the electrode-C.C interface and separator-Li foil interface increased from 708 to 3312 mol/m^3. When compared to the conventional structure, however, the 3D hybrid structure (Figures 7a to 7c) significantly reduced them by 96%, 95% and 46% more (270 µm, 380 µm, and 390 µm), respectively. As shown in Figures 7d to 7f, the HS structure also reduced the electrolyte concentration difference by 8%, 19%, and 21% (270 µm, 380 µm, and 390 µm, respectively). This implied that the 3D structure improved the transportation of ions inside the electrolyte and then enhanced the utilization of active materials. To obtain a clear idea of the advantages of a 3D hybrid structure, a case of flux distribution was plotted at 270 µm (shown in Figure 7g). The size of the arrow indicates a logarithmic scale of flux inside the structure. It can be observed that the flux of the 3D hybrid structure at the electrode-separator interface was five times stronger and gradually decreased toward the electrode-C.C. interface, and finally became similar to the flux of the conventional structure.

Less concentration development indicated higher material utilization. It also implied less stress development. To confirm this, a stress model was developed. This model assumed that the particles were spheres, so the stress developed in the particles had two components:

radial stress σ_r and tangential stress σ_t.

$$\sigma_r(r) = \frac{2\Omega_j E_j}{3(1-\nu_j)}\left(\frac{1}{R_j^3}\int_0^{R_j} c(r,t)\,r^2 dr - \frac{1}{r^3}\int_0^{r} c(r,t)\,r^2 dr\right) \quad [26]$$

$$\sigma_t(r) = \frac{\Omega_j E_j}{3(1-\nu_j)} \left(\frac{2}{R_j^3}\int_0^{R_j} c(r,t)\,r^2 dr - \frac{1}{r^3}\int_0^{r} c(r,t)\,r^2 dr - c(r,t)\right) \quad [27]$$

where $\tilde{c}$ is the concentration change from the initial value, ν_j is the Poisson's ratio, and E_j is the Young's modulus of active materials.[23] By considering a crack opening caused by the tangential component, Eq. 27 can be rewritten based on the concentration's analytical equations (Eqs. 5 and 7) as

$$\sigma_t(R_p, t) = \frac{\Omega_p E_p}{9(1-\nu_p)}\left(3c_{s,p,avg}(t) - 3c_{s,p,surf}(t)\right) \quad [28]$$

As an example, the case at 270 μm (shown in Figure 7h) was used to compare the distribution of stress of the active material particles. It was observed that the maximum particle stress inside the 3D hybrid structure (160 MPa) was 20% smaller than the one inside the conventional structure (190 MPa). This smaller stress development may have caused less mechanical failure, leading to a longer cycle life, which is another benefit of 3D structured electrodes.

Conclusions

In this work, a 3D computational model was developed to simulate a large-scale 3D battery electrode structure, based on the porous electrode theory with a 4th order analytical expression for solid phase concentration. Results obtained from the 3D model were compared with experimental observations of different electrode structures and thicknesses, based on voltage profiles and capacities. It was found that the solid phase concentration gradient in the electrode structure played an important role in the transport of species, and that the 3D structure reduced the concentration gradient. An analytical method was also developed to determine the limiting factors in diffusion and electrolyte transportation. Thickness and volume fraction were found to be key factors in battery structure design that determined battery performance. The developed model can be a very useful tool as a guideline for optimal 3D electrode designs.

Acknowledgment

The authors gratefully acknowledge the financial support from National Science Foundation Awards (CMMI-1563029/1747608, CBET-1510085).

ORCID

Xinhua Liang https://orcid.org/0000-0001-7979-0532
Rahul Panat https://orcid.org/0000-0002-4824-2936
Jonghyun Park https://orcid.org/0000-0003-4241-3842

References

1. K. G. Gallagher, S. E. Trask, C. Bauer, T. Woehrle, S. F. Lux, M. Tschech, P. Lamp, B. J. Polzin, S. Ha, B. Long, and Q. J. Wu, *The Electrochem. Soc*, **163**(2), A138 (2016).
2. T. S. Arthur, D. J. Bates, N. Cirigliano, D. C. Johnson, P. Malati, J. M. Mosby, E. Perre, M. T. Rawls, A. L. Prieto, and B. Dunn, *Mrs Bulletin*, **36**(7), 523 (2011).
3. S. Ferrari, M. Loveridge, S. D. Beattie, M. Jahn, R. J. Dashwood, and R. Bhagat, *J. Power Sources*, **286**, 25 (2015).
4. J. W. Long, B. Dunn, D. R. Rolison, and H. S. White, *Chemical Reviews*, **104**(10), 4463 (2004).
5. J. Li, M. C. Leu, R. Panat, and J. Park, *Materials & Design*, **119**, 417 (2017).
6. M. S. Saleh, J. Li, J. Park, and R. Panat, *Additive Manufactruing*, **23**, 70 (2018).
7. J. J. Adams, E. B. Duoss, T. F. Malkowski, M. J. Motala, B. Y. Ahn, R. G. Nuzzo, J. T. Bernhard, and J. A. Lewis, *Advanced Materials*, **23**(11), 1335 (2011).
8. D. S. Engstrom, B. Porter, M. Pacios, and H. Bhaskaran, *J. Materials Research*, **29**(17), 1792 (2014).
9. K. Fu, Y. Wang, C. Yan, Y. Yao, Y. Chen, J. Dai, S. Lacey, Y. Wang, J. Wan, T. Li, and Z. Wang, *Advanced Materials*, **28**(13), 2587 (2016).
10. K. Sun, T. S. Wei, B. Y. Ahn, J. Y. Seo, S. J. Dillon, and J. A. Lewis, *Advanced Materials*, **25**(33), 4539 (2013).
11. S. H. Kim, K. H. Choi, S. J. Cho, S. Choi, S. Park, and S. Y. Lee, *Nano letters*, **15**(8), 5168 (2015).
12. P. Priimägi, D. Brandell, S. Srivastav, A. Aabloo, H. Kasemägi, and V. Zadin, *Electrochimica Acta*, **209**, 138 (2016).
13. M. A. Martin, C. F. Chen, P. P. Mukherjee, S. Pannala, J. F. Dietiker, J. A. Turner, and D. Ranjan, *J. The Electrochem. Soc*, **162**(6), A991 (2015).
14. S. Das, J. Li, and R. Hui, In *Proceedings of the COMSOL Conference,* Boston, MA, USA, 2014, October. pp. 8.
15. S. Lee, A. M. Sastry, and J. Park, *J. Power Sources*, **315**, 96 (2016).
16. J. Park, J. Li, W. Lu, and A. M. Sastry, *J. Applied Physics*, **119**(2), 025101 (2016).
17. M. Doyle, J. Newman, A. S. Gozdz, C. N. Schmutz, and J. M. Tarascon, *J. The Electrochem. Soc*, **143**(6), 1890 (1996).
18. P. Albertus, J. Christensen, and J. Newman, *J. The Electrochem. Soc*, **156**(7), A606 (2009).
19. S. Golmon, K. Maute, and M. L. Dunn, *Computers & Structures*, **87**(23), 1567 (2009).
20. V. R. Subramanian, V. D. Diwakar, and D. Tapriyal, *J. The Electrochem. Soc*, **152**(10), A2002 (2005).
21. M. Doyle, T. F. Fuller, and J. Newman, *J. The Electrochem. Soc*, **140**(6), 1526 (1993).